Matter and Radiation at Extremes | RESEARCH ARTICLE | scitation.org/journal/mre

Mitigation of the ablative Rayleigh–Taylor instability by nonlocal electron heat transport

Cite as: Matter Radiat. Extremes 7, 055902 (2022); doi: 10.1063/5.0088058
Submitted: 12 February 2022 • Accepted: 24 July 2022 •
Published Online: 23 August 2022

Jun Li,[1] Rui Yan,[1,2,a)] Bin Zhao,[2,3] Jian Zheng,[2,4] Huasen Zhang,[5] and Xiyun Lu[1,a)]

AFFILIATIONS

[1] Department of Modern Mechanics, University of Science and Technology of China, Hefei 230026, China
[2] Collaborative Innovation Center of IFSA (CICIFSA), Shanghai Jiao Tong University, Shanghai 200240, China
[3] Department of Mathematics and Physics, Nanjing Institute of Technology, Nanjing, JiangSu 211167, China
[4] Department of Plasma Physics and Fusion Engineering, University of Science and Technology of China, Hefei, Anhui 230026, China
[5] Institute of Applied Physics and Computational Mathematics, Beijing 10094, China

[a)] **Authors to whom correspondence should be addressed:** ruiyan@ustc.edu.cn and xlu@ustc.edu.cn

ABSTRACT

The effects of electron nonlocal heat transport (NLHT) on the two-dimensional single-mode ablative Rayleigh–Taylor instability (ARTI) up to the highly nonlinear phase are reported for the first time through numerical simulations with a multigroup diffusion model. It is found that as well as its role in the linear stabilization of ARTI growth, NLHT can also mitigate ARTI bubble nonlinear growth after the first saturation to the classical terminal velocity, compared with what is predicted by the local Spitzer–Härm model. The key factor affecting the reduction in the linear growth rate is the enhancement of the ablation velocity V_a by preheating. It is found that NLHT mitigates nonlinear bubble growth through a mechanism involving reduction of vorticity generation. NLHT enhances ablation near the spike tip and slows down the spike, leading to weaker vortex generation as the pump of bubble reacceleration in the nonlinear stage. NLHT more effectively reduces the nonlinear growth of shorter-wavelength ARTI modes seeded by the laser imprinting phase in direct-drive laser fusion.

I. INTRODUCTION

Rayleigh–Taylor instability (RTI)[1,2] occurs when a fluid supports or accelerates another fluid of higher density. It plays a crucial role in many natural systems and engineering applications,[3,4] in particular in inertial confinement fusion (ICF),[5–7] which has recently reached an astonishing milestone toward the goal of ignition,[8,9] and in astrophysics.[10–12] RTI is an inevitable occurrence and causes severe performance degradation of ICF implosions as the laser energy irradiates the outer surface of a spherical capsule containing the fusion fuel, creating a hotter low-density plasma corona pushing onto the denser and colder shell. Modulations seeded by target roughness and laser nonuniformities can grow via RTI, thereby reducing target compression,[13] mixing ablator material into the fusion fuel,[14–17] and eventually degrading the neutron yield. RTI at ablative fronts (ARTI) is characterized by mass ablation driven by the laser energy deposited at the critical surface and then transported to the shell surface. It is well known that ablation stabilizes ARTI in the linear (i.e., exponential growth) phase.[18–24] When the mode amplitude exceeds a threshold fraction (around 0.1 as predicted by classical RTI theory[25,26]) of its wavelength, the exponential growth ceases, the nonlinear phase starts, and the modulations develop into "bubbles" (lighter fluid rising through the denser fluid) and "spikes" (denser fluid falling through the lighter fluid) owing to the generation of higher harmonics. The bubble velocity transitions to a constant terminal value[27,28] in the deep nonlinear phase of the classical RTI. This transition is commonly known as "nonlinear saturation." It has been found that ablation will expand the nonlinear saturation threshold fraction from 0.1 up to 0.3 for shorter-wavelength modes according to nonlinear ARTI theory.[29,30] In the highly nonlinear phase, ablation will destabilize ARTI bubble growth owing to the vortex acceleration mechanism,[31,32] accelerating the bubble to a velocity well above the classical terminal value. The ARTI bubbles are accelerated by the centrifugal force provided by vortices when

penetrating through the dense shell, compromising shell integrity in ICF implosions.

Accurate modeling of thermal transport in ICF plasmas is required for predicting the key processes critical to ignition target design, one of which is the growth of ARTI.[33] In low-Z materials like deuterium–tritium (DT), where radiation energy is negligible, thermal transport is mainly via electrons. The electron conduction model implemented in general radiation-hydrodynamic codes is based on the classical Spitzer–Härm (SH) theory:[34] $\boldsymbol{Q}_{\mathrm{SH}} = -\kappa_{\mathrm{SH}} \nabla T_e$, where $\boldsymbol{Q}_{\mathrm{SH}}$ is the SH heat flux vector, T_e is the electron temperature, and $\kappa_{\mathrm{SH}} \propto T_e^{5/2}$ is the SH thermal conductivity coefficient. The SH model starts from the following first-order expansion of the electron distribution function (EDF):

$$f_e(\boldsymbol{v}) = f_0(v) + \frac{\boldsymbol{v}}{v} \cdot \boldsymbol{f}_1(v), \tag{1}$$

where $f_0(v)$ is the isotropic part of the EDF, which is assumed to be the usual Maxwell–Boltzmann distribution, $\boldsymbol{v}$ is the velocity of electron thermal motion, and $(\boldsymbol{v}/v) \cdot \boldsymbol{f}_1(v)$ is the first-order anisotropic part of the EDF. The heat flux is determined by $\boldsymbol{f}_1$. The SH model is local, since the heat flux is determined by the local plasma quantities. Unfortunately, this simple SH model fails to reproduce experimental data. The temperature gradients in ICF plasmas are sufficiently large that the assumption of the SH model that the mean free path of high-energy heat-carrying electrons is much smaller than the scale length of the temperature gradient $[L_T \equiv |\nabla \ln(T_e)|^{-1}]$ breaks down in such regions. These high-energy electrons escape steep temperature gradients, causing both classical local heat flux reduction and nonlocal preheating ahead of the temperature front. It is usually suggested that the electron nonlocal heat transport (NLHT) needs to be taken into account when the Knudsen number $Kn \equiv \lambda_{ei}/L_T \geq 0.01$,[35–38] where λ_{ei} is the electron–ion (e–i) mean free path. Because heat transport modeling affects mass ablation processes, it will also modify ARTI evolution. Discrepancies between experiments and standard SH simulations were observed in a number of pioneering works.[39–43] It was shown that simulations without NLHT predicted faster RTI growths in the linear phase than were observed experimentally[39–42] and that accounting for NLHT led to considerably better agreement between the simulated RTI growth rates[39,40,42,43] and experiments. The NLHT linear stabilization was mostly attributed to a one-dimensional (1D) preheating effect caused by penetration of the high-energy electrons from the tail of the Maxwellian distribution into the high-density target,[39,40,42–44] which causes a lower target peak density and a longer density scale length in the longitudinal hydrodynamic profiles. Although the influence of NLHT on the ARTI linear growth rates can be estimated phenomenologically by substituting the 1D hydrodynamic parameters modified by NLHT into the existing linear theories based on the SH model,[18–21] its effect on ARTI evolution in the nonlinear phase is unknown, leading to risky uncertainties in ICF designs.

Modeling NLHT is challenging at ICF-relevant temporal and spatial scales. The most accurate thermal transport models solve the Vlasov–Fokker–Planck (VFP) kinetic equations,[35] but are usually too computationally expensive in multiple dimensions. Instead, an *ad hoc* heat flux limiter[45] is often employed to take account of flux inhibition effects in hydrodynamic codes to match certain aspects of experimental results. However, a flux limiter cannot capture preheating physics. More recently, the nonlocal multigroup diffusion model proposed by Schurtz, Nicolaï, and Busquet (the SNB model)[46] has been considered as a method that balances physical accuracy and computational efficiency. When NLHT effects are significant, f_0 in Eq. (1) will deviate from the Maxwell–Boltzmann distribution, and $\boldsymbol{f}_1$ will deviate from its counterpart in the SH model. Starting from the steady VFP equation with the Bhatnagar, Gross, and Krook (BGK) collisional operator,[47] the SNB model gives a set of transport equations that can be solved for the deviation of f_0 from the Maxwell–Boltzmann distribution. More details of the SNB model are given in Sec. II. SNB-like algorithms have been extensively tested[48–51] and used in state-of-the-art ICF codes.

In this paper, we present for the first time a numerical simulation of ARTI evolution with NLHT up to the highly nonlinear phase and uncover a new nonlinear bubble mitigation mechanism due to the reduction of vorticity generation by NLHT. NLHT suppresses vorticity generation by inhibiting the growth of spikes, which in turn suppresses the nonlinear acceleration of bubbles. This newly discovered physical mechanism allows for a better understanding of the effect of NLHT on the evolution of nonlinear ARTI in high-energy-density environments. The results described here can help to understand and evaluate the differences between experimental data and current numerical simulations and lead to better strategies for providing the necessary margin in ICF design.

II. SIMULATION SETUP

Our simulations are performed using the hydrodynamic code *ART*,[31,32] dedicated to simulating ARTI in ICF-relevant regimes.[31,32,52–54] *ART* solves the single-fluid hydrodynamic equations over a Cartesian grid, with switchable SH and SNB heat transport models being implemented. For each time step, the mass equation, the momentum equation, and the energy equation without thermal transport are first solved explicitly using a finite volume approach:

$$\frac{\partial \rho}{\partial t} + \nabla \cdot (\rho \boldsymbol{u}) = 0, \tag{2}$$

$$\frac{\partial (\rho \boldsymbol{u})}{\partial t} + \nabla \cdot (\rho \boldsymbol{u}\boldsymbol{u}) = -\nabla P + \rho \boldsymbol{g}, \tag{3}$$

$$\frac{\partial E}{\partial t} + \nabla \cdot [(P + E)\boldsymbol{u}] = \rho \boldsymbol{g} \cdot \boldsymbol{u}, \tag{4}$$

where ρ, $\boldsymbol{u}$, P, and $\boldsymbol{g}$ are the density, velocity, pressure, and acceleration, respectively. $E \equiv [P/(\gamma - 1)] + \rho|\boldsymbol{u}|^2/2$ is the total energy, where $\gamma = 5/3$ is the ratio of specific heats. The spatial reconstruction is performed using the MUSCL (Monotone Upstream-centered Schemes for Conservation Laws)–Hancock scheme,[55] and the Riemann problem at the cell interfaces is approximately solved using the Harten–Lax–van Leer–contact (HLLC)[56] solver. The thermal transport part of the energy equation is then treated implicitly to

avoid the strict time step requirement of explicit diffusion equation solvers:

$$\rho C_v \frac{\partial T_e}{\partial t} = -\nabla \cdot \mathbf{Q}, \tag{5}$$

where C_v is the specific heat at constant volume and $\mathbf{Q}$ is the SH or SNB heat flux vector. A pressure correction due to thermal conduction is then made.

The SNB model implemented in *ART* divides electrons of different energies (mean free paths) into a number of groups and for each group solves a transport equation for H_g proportional to the deviation of the electron distribution from Maxwellian on the given density and temperature profiles:

$$\left[\frac{1}{\lambda_g(\boldsymbol{r})} - \nabla \cdot \frac{\lambda_g(\boldsymbol{r})}{3}\nabla\right] H_g(\boldsymbol{r}) = -\nabla \cdot \boldsymbol{U}_g(\boldsymbol{r}). \tag{6}$$

Here, $\boldsymbol{U}_g$ is defined as

$$\boldsymbol{U}_g \equiv \frac{\mathbf{Q}_{\mathrm{SH}}}{24} \int_{E_{g-1}/k_{\mathrm{B}}T_e}^{E_g/k_{\mathrm{B}}T_e} \beta^4 e^{-\beta}\, d\beta, \tag{7}$$

where λ_g is the mean free path, E_g is the upper energy bound of the gth group, and k_{B} is Boltzmann's constant. The SNB heat flux is derived as $\mathbf{Q}_{\mathrm{SNB}} = \mathbf{Q}_{\mathrm{SH}} - \sum_g \lambda_g \nabla H_g/3$, where $\mathbf{Q}_{\mathrm{SH}}$ is the SH heat flux calculated on the basis of the given density and temperature profiles. Cao *et al.*[51] found that $\nabla \cdot \mathbf{Q}_{\mathrm{SNB}} = -\sum_g H_g/\lambda_g$, and this relation can be directly employed when solving the thermal transport equation. The SNB module is used to update the hydrodynamic quantities using a predictor/corrector implicit iterative algorithm similar to that of Cao *et al.*[51] and has been validated with Refs. 48 and 57.

To study the growth of small-scale ARTI in the acceleration phase of ICF implosion when the aspect ratio is large, the planar-target approximation is valid and the simulation uses a rectangular computational domain in the x–z plane. For the quasi-equilibrium state in the z direction from which the ARTI perturbations grow, a profile typical of a direct-drive National Ignition Facility (NIF) target is used, as illustrated in Fig. 1(a). The initial ablation front (the interface between the dense and the ablated plasma) is located at z_a and the peak density is $\rho_a = 4$ g/cm^3. The quasi-equilibrium state with the SH model is obtained by integrating the 1D hydrodynamic equilibrium equations in the frame of reference of the shell from the ablation front toward both sides. Our simulations do not include the low-density region where the lasers are interacting with the plasma, and therefore we do not directly handle laser absorption. Instead, the laser energy transported toward the ablation front is simulated by a constant bottom-boundary heat flux calculated self-consistently with the SH model on the basis of the 1D hydrodynamic profiles to ablate the target at an ablation velocity $V_a = 3.5$ μm/ns (i.e., the penetration velocity of the ablation front into the heavy shell material), and the corresponding ablation pressure (the pressure at the ablation surface) is $P_a = 130$ Mbar. The quasi-equilibrium state with the SNB model is initialized using the SH hydrodynamic profiles and evolves self-consistently with the SNB model. The SNB

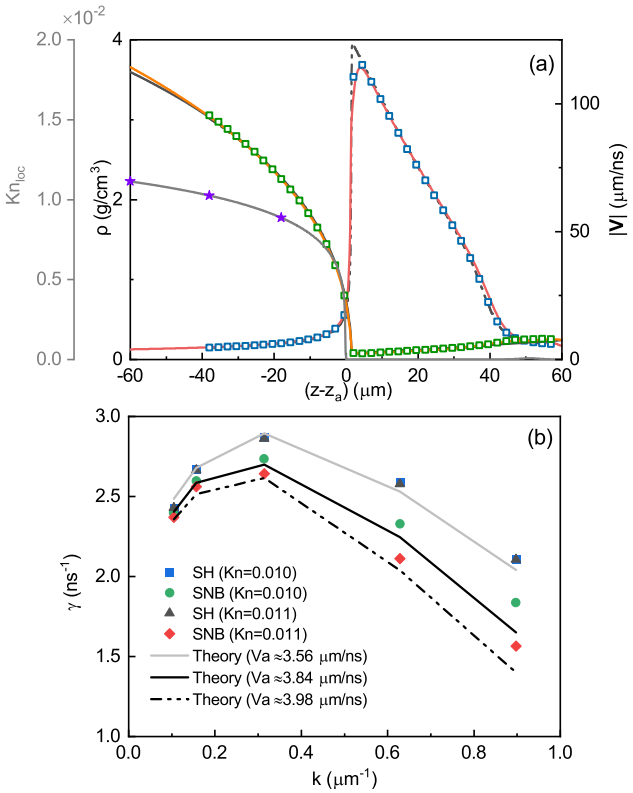

FIG. 1. (a) Equilibrium hydrodynamic profiles of a 1.5 MJ NIF ignition target during the acceleration phase after evolving for 1 ns using the initialization of the SH model: density from the SH model (black dashed line) and from the SNB model for $Kn = 0.01$ (blue squares) and $Kn = 0.011$ (red solid line); v_z from the SH model (black solid line) and from the SNB model for $Kn = 0.01$ (green squares) and $Kn = 0.011$ (orange solid line). The local Knudsen number Kn_{loc} profile (gray solid line) at $t = 0$ is also plotted. The three purple stars mark the locations of $Kn_{\mathrm{loc}} = \{0.011, 0.010, 0.009\}$. (b) Linear growth rates of ARTI from the SH and SNB models for different values of Kn: the SH model for $Kn = 0.01$ (blue squares) and $Kn = 0.011$ (black triangles) and the SNB model for $Kn = 0.01$ (green circles) and $Kn = 0.011$ (red diamonds). The black triangles and blue squares are superimposed, since the SH model is local and independent of Kn. The theoretical curves are $\gamma = (A_T kg - A_T^2 k^2 V_a^2/r_d)^{1/2} - (1 + A_T)kV_a$.[20]

and SH heat fluxes are kept the same at the bottom boundary by setting the reflective boundary condition $\partial_z H_g = 0$. To adjust the strength with which NLHT modifies the 1D hydrodynamic profiles, our simulations are designed with different values of Kn. The characteristic Kn in each simulation is chosen as the maximum local Knudsen number in the system occurring at the bottom boundary, and Kn can be increased by extending the bottom boundary of the simulation box toward the critical surface. The distance L from the bottom boundary ($z = 0$) to the ablation surface ($z = z_a$) is set to $\{38, 60\}$ μm, corresponding to $Kn = \{0.010, 0.011\}$. Expanding L from 38 μm to 60 μm not only increases Kn by 10%, but also significantly expands the spatial region in which the nonlocality condition is satisfied (nonlocal effects are usually considered important[35–38] when $Kn \gtrsim 10^{-2}$), since Kn increases slowly with L [see the local Knudsen number profile in Fig. 1(a)]. The larger-Kn case is expected

to exhibit more significant NLHT modifications of the 1D hydrodynamic profiles near the ablation front, as shown in Fig. 1(a). A simulation is also performed for another case with shorter L (18 μm, yielding $Kn = 0.009$), and NLHT is expected to be even weaker in this case.

The gravity is initialized as $g_0 = 110$ μm/ns^2. Since the shell mass decreases owing to ablation, the effective acceleration $g(t)$ is slowly and automatically adjusted in time during the simulation to keep the ablation front approximately fixed in space, i.e., $g(t) = [(P + \rho u^2)_{\text{lower}} - (P + \rho u^2)_{\text{upper}}]/M_s$, where the subscripts "lower" and "upper" indicate the integral values at the bottom and top boundaries, respectively, and M_s is the mass of the remaining plasma in the computational domain. This is equivalent to studying the ARTI growth in the frame of the shell. The RTI is seeded via velocity perturbations at the ablation front in the form $V_{pz} = V_{p0}\cos(kx)\exp(-k|z|)$, $V_{p0}/V_a = 0.286$. The simulations are performed for a series of wavelengths $\lambda \equiv 2\pi/k$. The grid size is $\Delta x = \Delta z = 0.1$ μm. Periodic boundary conditions are applied along the x direction, and inflow and outflow boundary conditions are applied on the upper and lower boundaries, respectively, in the z direction.

III. RESULTS AND DISCUSSION

The linear growth rates are found to be reduced by NLHT through its enhancement of the ablation velocity V_a due to stronger preheating. The ARTI amplitudes η in the simulations are measured as half of the peak-to-valley heights. The linear growth rate is fitted with data in the exponential-growth stage when $\eta \le 0.1\lambda$ (below which ARTI is usually considered in the linear phase) for a series of wavelengths [see Fig. 1(b)]. The theoretical growth rate curves for comparison are calculated using $\gamma = (A_T kg - A_T^2 k^2 V_a^2/r_d)^{1/2} - (1 + A_T)kV_a$,[20] where $r_d = \rho_l/\rho_h$ is the density ratio between the effective light (ρ_l) and heavy (ρ_h) fluids, and $A_T \equiv (\rho_h - \rho_l)/(\rho_h + \rho_l)$ is the effective Atwood number. Since the density varies continuously, it is necessary to define appropriate densities for the light and heavy fluids, according to Eqs. (5) and (6) in Ref. 20: $\rho_h \approx \rho_a$ and $\rho_l \approx \rho_a \mu_0 (kL_0)^{1/\nu}$, where $L_0 = L_m \nu^\nu/(\nu + 1)^{\nu+1}$ is the characteristic thickness of the ablation front, $L_m = \min[|\rho/(\partial\rho/\partial x)|]$ is the minimum density gradient scale length, $\mu_0 = (2/\nu)^{1/\nu}/\Gamma(1 + 1/\nu) + 0.12/\nu^2$, ν is the thermal conduction power index, and $\Gamma(x)$ is the gamma function. The theoretical curves for the SNB cases are calculated using the same Atwood number A_T and density scale length L_0 as in the SH cases, together with the measured V_a in each individual SNB simulation. The fairly good agreement between theory and simulations that can be achieved by adjusting V_a alone is an indication that enhanced V_a is the key factor lowering the linear growth rates. The enhancement of V_a is attributed to the enhanced heat flux and reduced peak density at the ablation front caused by preheating. The growth rate differences between SNB and SH cases are more significant for larger Kn. The linear growth rate in the $Kn = 0.009$ case is found to be closer to that in the SH case.

In the $Kn = 0.01$ case, although the linear growth rates are reduced by NLHT, the slowdowns of bubbles and spikes are different. As shown in Fig. 2(a), the SNB spike trajectory deviates from the SH case earlier than the bubble trajectories. By $t = 2$ ns [i.e., $Z_t = 253$ μm, where $Z_t \equiv \int_0^t \int_0^{t''} g(t')\,dt'\,dt''$ is the displacement function commonly used instead of time to compensate for slight variations of gravity], when the ARTI amplitude is large enough to be considered to be in the nonlinear stage, the bubble trajectories from the two models are still close, indicating

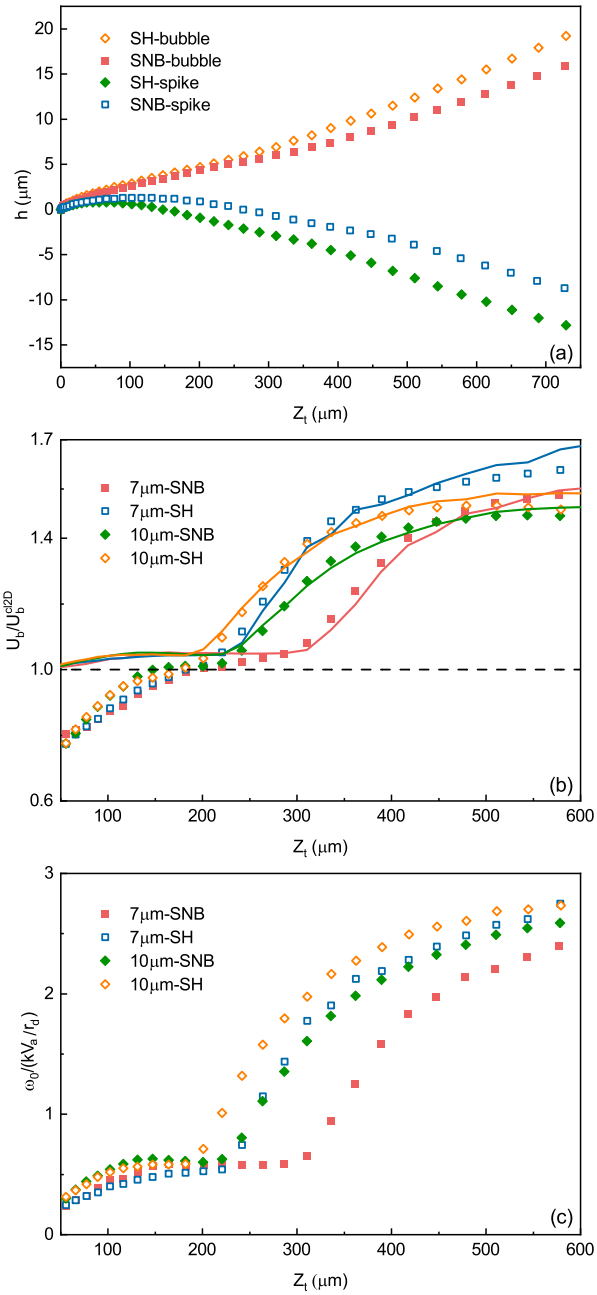

FIG. 2. (a) Bubble and spike trajectories from the SH and SNB models vs Z_t in the $\lambda = 7$ μm, $Kn = 0.01$ cases, where $Z_t \equiv \int_0^t \int_0^{t''} g(t')\,dt'\,dt''$ is the displacement function commonly used in theoretical descriptions of time-dependent acceleration histories. (b) Ratio of bubble velocities to classical values. The symbols represent the simulations and the curves are from the analytical model given by Eq. (8). (c) Average vorticity inside the bubble volume within a length $1/k$ below the bubble vertex, as illustrated in Fig. 3(a).

nonuniform ablation of bubbles and spikes by the nonlocal heat flux. In the $Kn = 0.011$ case, which is not shown in Fig. 2(a), it is found that stronger preheating reduces bubble growth in the linear stage. Therefore, the $Kn = 0.01$ cases allow us to focus on the NLHT effects on nonlinear bubble evolution while minimizing the impact on bubble linear growth caused by 1D preheating effects on the hydrodynamic profiles.

The ARTI bubble velocity U_b, defined as the speed with which the bubble vertex penetrates through the slab of dense fluid, is plotted in Fig. 2(b) for two different unstable perturbation wavelengths close to the linear cutoff ($\lambda > \lambda_{\text{cutoff}} \approx 6\ \mu$m) and two different thermal transport models. The bubble velocities start to grow from the values of V_a in each individual case. As the bubble amplitude becomes larger, the low-density plasma filling the bubble is cooled down by the cold walls containing the bubble, and the mass ablation from the bubble walls becomes negligible. At this stage, the bubble behaves as in the classical RTI case without ablation, and the bubble velocity saturates at the two-dimensional (2D) classical value $U_b^{\text{cl2D}} = [g(1 - r_d)/(3k)]^{1/2}$ given by potential-flow theory,[27,28] as shown in Fig. 2(b). The ratio U_b/U_b^{cl2D} approaches 1 as ARTI saturates. There is little difference between the values of U_b from the SH and SNB models up to this stage, which is consistent with the fact that the bubble trajectories in the linear phase have not been significantly affected by switching from SH to SNB in the $Kn = 0.01$ case.

Switching heat transport models alters the bubble reacceleration processes after the first saturation of U_b to U_b^{cl2D}, as plotted in Fig. 2(b). With both thermal transport models, the simulations show that the vortex carried by the material ablated from the spike is transported into the bubble and accumulates near the bubble vertex as the ablated plasma fills the bubble volume. The vortex then provides a centrifugal force that raises the bubble vertex and accelerates U_b beyond U_b^{cl2D}, i.e., reacceleration occurs. NLHT causes a reduction in bubble reacceleration. It is found that smaller-wavelength modes are more susceptible to NLHT, because the reacceleration stage is more strongly affected by NLHT in the 7 μm case [Fig. 2(b)]. Simulations have also been performed for larger perturbation wavelengths, and it has been found that the difference between the bubble velocities from the SNB and SH models is much smaller for λ greater than 20 μm.

Reduction of bubble reacceleration with the SNB model is consistent with the weaker vorticity accumulation inside the bubble plotted in Fig. 2(c). The vorticity ω_0 in Fig. 2(c) is the volume average of $\nabla \times \boldsymbol{u}$ inside the bubble between $1/k$ below the bubble vertex and the vertex, as shown in Fig. 3(a). With both thermal transport models, the nonlinear evolution of the bubble velocities can be approximated well by the asymptotic bubble velocity formula given in Ref. 31:

$$U_b^{\text{rot2D}} = \left[\frac{g(1 - r_d)}{3k} + r_d \frac{\omega_0^2}{4k^2}\right]^{1/2}. \tag{8}$$

A comparison of the simulations with the result from Eq. (8) is shown in Fig. 2(b). This indicates that the vorticity is also the key reason for the reacceleration in the SNB cases. The vorticity growth with the SNB model is slower than that with the SH model, and this effect is more significant for smaller-wavelength cases.

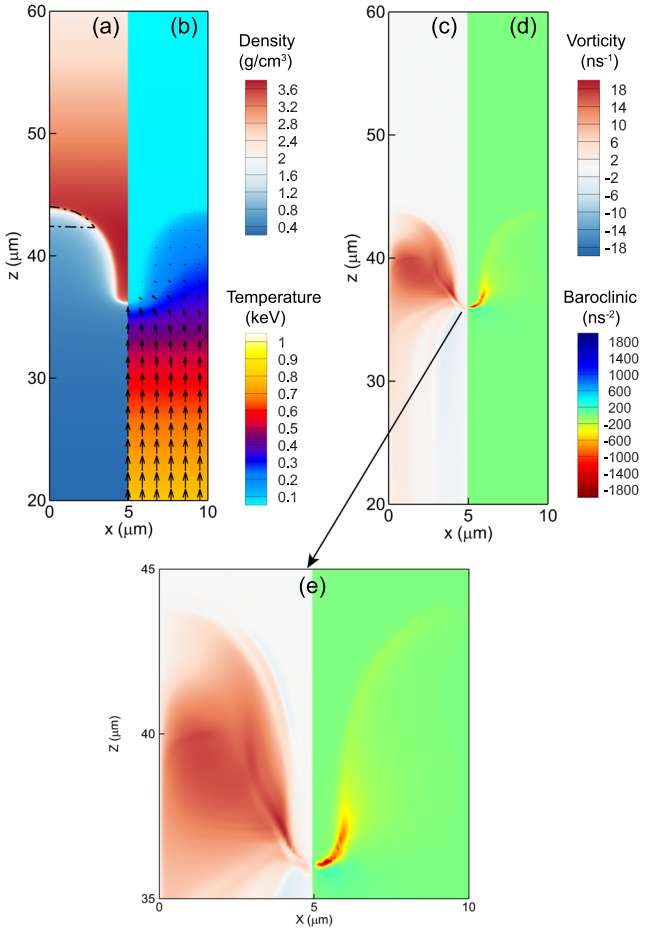

FIG. 3. Simulation results for the 10 μm-SNB case at $t = 1.7$ ns ($Z_t = 180\ \mu$m). (a) Density. The volume marked inside the bubble is within $1/k$ below the bubble tip. (b) Temperature contour with heat flux vectors. (c) Vorticity. (d) Baroclinic source $\dot{\omega}_{\text{baro}} \equiv -\nabla P \times \nabla\rho/\rho^2$. (e) Zoomed-in image of the vorticity and baroclinic source near the RTI interface. The hydrodynamic contours in the SH case are qualitatively similar to those in the SNB case.

The vorticity is generated in the region where ablation is significant. As the bubble and spike grow, the hot plasma inside the bubble is cooled down by the shell plasma. As a consequence, the majority of the heat flux can hardly enter the inside of the bubble, and mass ablation is predominant at the spike tip. Figure 3(a) shows the long bubble-spike structure. The mushroom-like structures usually seen in classical RTI near the spike tip are suppressed in ARTI owing to intense ablation. Figure 3(b) shows the temperature contours, and it can be seen that the heat flux vectors illustrated by arrows are mainly around and below the spike tip. The evolution of vorticity obeys $D\omega/Dt \equiv \partial\omega/\partial t + (\boldsymbol{u} \cdot \nabla)\omega = -\nabla P \times \nabla\rho/\rho^2$, with compressibility and viscosity effects neglected. The right-hand side, known as the baroclinic term, is recognized as the major source generating vorticity in ARTI. The vorticity filling the bubble [Fig. 3(c)] is originally driven by the baroclinic source [Fig. 3(d)] concentrated near the spike tip and is affected by the ablation process there.

The ablation process near the spike is affected by heat transport modeling and influences the falling speed of the spike. The SNB model produces larger heat fluxes in the ablation region than the SH model. In Fig. 4(a), the SNB correction to the heat flux along the axis of the spike in the $\lambda = 7$ μm SNB case is plotted. With the SNB model, there is a heat flux increase as a preheating effect in the coronal plasma. The SNB heat flux tunnels further through the high-density spike and causes a 35-fold increase compared with the SH heat flux near the sharp-density-gradient spike interface. Larger heat fluxes near the interface at the spike tip cause greater ablation of the spike and slow down the spike speed. This spike slowdown, which is visible from the linear stage to the deeply nonlinear stage [Fig. 2(a)], is found to be more significant for $\lambda = 7$ μm than for 10 μm. This trend is consistent with stronger ablation stabilization of smaller-wavelength perturbations in the linear phase of ARTI.

The baroclinic source is found to be largely correlated with the dimensionless quantity kL_{spike} in our simulations, where L_{spike} is the spike height defined as the vertical distance between the bubble and spike interfaces. The volume-averaged baroclinic term $\dot{\omega}_{baro}$ is found to have a linear dependence on kL_{spike} until the late stage of the simulations, as shown in Fig. 4(b). It can also be seen from Fig. 4(b) that this dependence is insensitive to the heat transport model used. Therefore, a lower spike speed leads to weaker vortex generation, which further reduces the bubble velocity via the vortex acceleration mechanism.

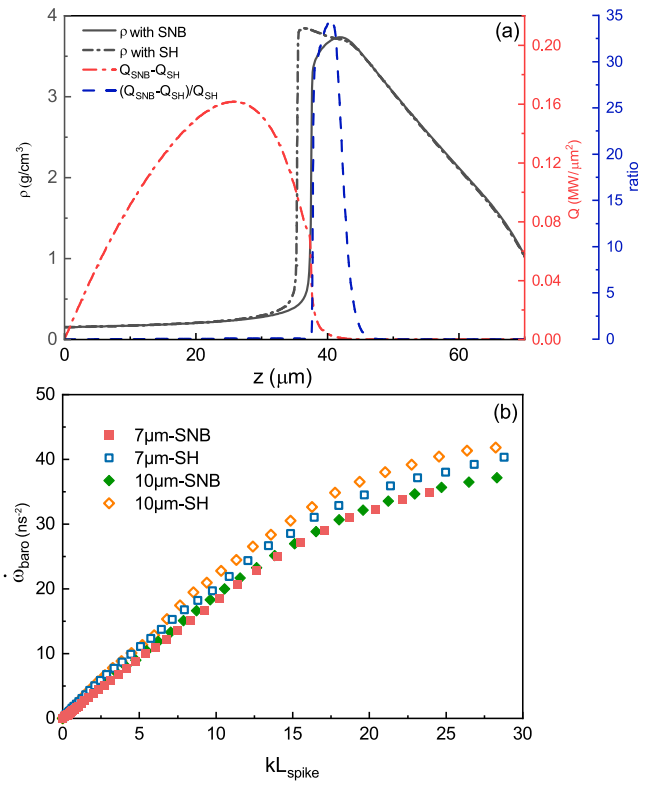

FIG. 4. (a) Density profile and the heat flux correction term $Q_{SNB} - Q_{SH}$ along the spike axis at $t = 2.1$ ns ($Z_t = 286$ μm) in the 7 μm SNB case. The density profile of the SH case at the same time is plotted as the dash-dotted line for comparison. Q_{SNB} and Q_{SH} are calculated using the density and temperature profiles from the SNB model. (b) Dependence of the volume-averaged baroclinic source $-\nabla P \times \nabla\rho/\rho^2$ on the dimensionless quantity kL_{spike} for both SH and SNB simulations.

In our 2D simulations with the SH model, both the bubble velocity and the vorticity inside the bubble saturate in the highly nonlinear phase,[31,32] as also shown in Figs. 2(b) and 2(c). It can be seen that the NLHT effect in the SNB cases leads to a slower vorticity accumulation inside the bubble, while the bubble velocity may still approach a vortex-accelerated terminal velocity similar to that in the SH case. Given adequate growth time in the SNB case, the slowed-down vorticity generation $\dot{\omega}_{baro}$ grows larger as L_{spike} grows [see Fig. 4(b)], and thus the vorticity accumulated inside the bubble is likely to increase to a similar saturation value as in the SH case [see Fig. 2(c)].

IV. CONCLUDING REMARKS

In summary, it has been shown that NLHT can mitigate ARTI growth in both its linear and nonlinear stages. The strength of the effect of NLHT on the ablation front is varied by adjusting the characteristic Kn. For $Kn \sim 10^{-2}$, the key factor reducing the linear growth rate is the enhanced V_a. The reduction in linear growth rate is found to be due more to slowdown of spikes than to that of bubbles, since NLHT causes greater ablation of spikes than of bubbles. For $Kn = 0.01$, the linear phase of spike growth is inhibited by NLHT, but the linear phase of bubble growth is minimally affected, and thus study of this regime can help isolate the NLHT effects on bubble nonlinear growth, which is a 2D effect that cannot be predicted by a 1D hydrodynamic simulation. It has been found that NLHT enhances the ablation near the side of the spike tip and slows down the spike. Since the spike height is correlated with the vorticity generation rate, the nonlinear bubble reacceleration due to the vortex generated near the spike tip and transported into the bubble is reduced by NLHT. This newly discovered mechanism is more significant for smaller-wavelength modes and can be utilized to suppress the nonlinear bubble growth of short-wavelength ARTI seeded by the laser imprinting phase in direct-drive laser fusion. The controlled use of NLHT has already attracted some research interest. Otani *et al.*[58] utilized "cocktail color irradiation" to mitigate RTI by moderately enhancing NLHT. Our findings may help optimize those strategies utilizing NLHT to mitigate RTI in ICF-relevant experiments.

In the presence of intense vorticity generation accompanied with ARTI, the self-generated magnetic field is also expected to be intense,[59,60] because the self-generated magnetic field is closely related to the vorticity (and the baroclinic term). The combined influence of self-generated magnetic fields and electron NLHT[61] on ARTI evolution is an interesting topic. Important related topics, such as bubble merger and competition, convergent geometry, three-dimensional effects, and coupling with radiation transport should be studied in future work.

ACKNOWLEDGMENTS

This research was supported by Science Challenge Project No. TZ2016001, by the Strategic Priority Research Program of Chinese Academy of Sciences under Grant Nos. XDA25050400,

XDA25010200, and XDB16000000, by the National Natural Science Foundation of China (NSFC) under Grant Nos. U1530261, 12175229, and 11621202, and by the Fundamental Research Funds for the Central Universities. Some of the numerical calculations in this paper were performed on the supercomputing system at the Supercomputing Center of the University of Science and Technology of China.

AUTHOR DECLARATIONS

Conflict of Interest

The authors have no conflicts to disclose.

Author Contributions

Jun Li: Conceptualization (equal); Data curation (lead); Formal analysis (lead); Investigation (lead); Methodology (lead); Software (lead); Validation (lead); Visualization (lead); Writing – original draft (lead); Writing – review & editing (equal). **Rui Yan**: Funding acquisition (lead); Investigation (supporting); Methodology (supporting); Project administration (lead); Resources (lead); Supervision (lead); Writing – original draft (supporting); Writing – review & editing (lead). **Bin Zhao**: Software (supporting); Validation (supporting). **Jian Zheng**: Supervision (supporting); Writing – review & editing (supporting). **Huasen Zhang**: Formal analysis (supporting); Writing – review & editing (supporting). **Xiyun Lu**: Formal analysis (supporting), Funding acquisition (lead); Project administration (equal); Supervision (equal), Writing – review & editing (supporting).

DATA AVAILABILITY

The data that support the findings of this study are available from the corresponding author upon reasonable request.

REFERENCES

[1]L. Rayleigh, *Scientific Papers II* (Cambridge University Press, Cambridge, England, 1900), p. 200.
[2]G. I. Taylor, "The instability of liquid surfaces when accelerated in a direction perpendicular to their planes. I," Proc. R. Soc. London, Ser. A **201**, 192–196 (1950).
[3]Y. Zhou, "Rayleigh–Taylor and Richtmyer–Meshkov instability induced flow, turbulence, and mixing. I," Phys. Rep. **720–722**, 1–136 (2017).
[4]Y. Zhou, "Rayleigh–Taylor and Richtmyer–Meshkov instability induced flow, turbulence, and mixing. II," Phys. Rep. **723–725**, 1–160 (2017).
[5]J. D. Lindl, *Inertial Confinement Fusion* (Springer, New York, 1998).
[6]S. Atzeni and J. Meyer-ter-Vehn, *The Physics of Inertial Fusion: Beam Plasma Interaction Hydrodynamics, Hot Dense Mater* (Oxford University, 2004).
[7]R. Betti and O. A. Hurricane, "Inertial-confinement fusion with lasers," Nat. Phys. **12**, 435–448 (2016).
[8]A. B. Zylstra, O. A. Hurricane, D. A. Callahan, A. L. Kritcher, J. E. Ralph, H. F. Robey, J. S. Ross, C. V. Young, K. L. Baker, D. T. Casey *et al.*, "Burning plasma achieved in inertial fusion," Nature **601**, 542–548 (2022).
[9]A. Kritcher, C. Young, H. Robey, C. Weber, A. Zylstra, O. Hurricane, D. Callahan, J. Ralph, J. Ross, K. Baker, D. Casey, D. Clark, T. Döppner, L. Divol, M. Hohenberger, L. Hopkins, S. Pape, N. Meezan, and A. Pak, "Design of inertial fusion implosions reaching the burning plasma regime," Nat. Phys. **18**, 251 (2022).
[10]A. Burrows, "Supernova explosions in the universe," Nature **403**, 727–733 (2000).
[11]V. N. Gamezo, A. M. Khokhlov, E. S. Oran, A. Y. Chtchelkanova, and R. O. Rosenberg, "Thermonuclear supernovae: Simulations of the deflagration stage and their implications," Science **299**, 77 (2003).
[12]C. C. Kuranz, H. S. Park, C. M. Huntington, A. R. Miles, B. A. Remington, T. Plewa, M. R. Trantham, H. F. Robey, D. Shvarts, A. Shimony, K. Raman, S. MacLaren, W. C. Wan, F. W. Doss, J. Kline, K. A. Flippo, G. Malamud, T. A. Handy, S. Prisbrey, C. M. Krauland, S. R. Klein, E. C. Harding, R. Wallace, M. J. Grosskopf, D. C. Marion, D. Kalantar, E. Giraldez, and R. P. Drake, "How high energy fluxes may affect Rayleigh–Taylor instability growth in young supernova remnants," Nat. Commun. **9**, 1564 (2018).
[13]D. T. Casey, J. L. Milovich, V. A. Smalyuk, D. S. Clark, H. F. Robey, A. Pak, A. G. MacPhee, K. L. Baker, C. R. Weber, T. Ma, H.-S. Park, T. Döppner, D. A. Callahan, S. W. Haan, P. K. Patel, J. L. Peterson, D. Hoover, A. Nikroo, C. B. Yeamans, F. E. Merrill, P. L. Volegov, D. N. Fittinghoff, G. P. Grim, M. J. Edwards, O. L. Landen, K. N. Lafortune, B. J. MacGowan, C. C. Widmayer, D. B. Sayre, R. Hatarik, E. J. Bond, S. R. Nagel, L. R. Benedetti, N. Izumi, S. Khan, B. Bachmann, B. K. Spears, C. J. Cerjan, M. Gatu Johnson, and J. A. Frenje, "Improved performance of high areal density indirect drive implosions at the National Ignition Facility using a four-shock adiabat shaped drive," Phys. Rev. Lett. **115**, 105001 (2015).
[14]S. P. Regan, R. Epstein, B. A. Hammel, L. J. Suter, H. A. Scott, M. A. Barrios, D. K. Bradley, D. A. Callahan, C. Cerjan, G. W. Collins, S. N. Dixit, T. Döppner, M. J. Edwards, D. R. Farley, K. B. Fournier, S. Glenn, S. H. Glenzer, I. E. Golovkin, S. W. Haan, A. Hamza, D. G. Hicks, N. Izumi, O. S. Jones, J. D. Kilkenny, J. L. Kline, G. A. Kyrala, O. L. Landen, T. Ma, J. J. MacFarlane, A. J. MacKinnon, R. C. Mancini, R. L. McCrory, N. B. Meezan, D. D. Meyerhofer, A. Nikroo, H. S. Park, J. Ralph, B. A. Remington, T. C. Sangster, V. A. Smalyuk, P. T. Springer, and R. P. Town, "Hot-spot mix in ignition-scale inertial confinement fusion targets," Phys. Rev. Lett. **111**, 045001 (2013).
[15]J. Lindl, O. Landen, J. Edwards, and E. Moses, "Review of the National Ignition Campaign 2009–2012," Phys. Plasmas **21**, 020501 (2014).
[16]O. A. Hurricane, D. A. Callahan, D. T. Casey, P. M. Celliers, C. Cerjan, E. L. Dewald, T. R. Dittrich, T. Döppner, D. E. Hinkel, L. F. B. Hopkins, J. L. Kline, S. Le Pape, T. Ma, A. G. MacPhee, J. L. Milovich, A. Pak, H.-S. Park, P. K. Patel, B. A. Remington, J. D. Salmonson, P. T. Springer, and R. Tommasini, "Fuel gain exceeding unity in an inertially confined fusion implosion," Nature **506**, 343–348 (2014).
[17]C. R. Weber, T. Döppner, D. T. Casey, T. L. Bunn, L. C. Carlson, R. J. Dylla-Spears, B. J. Kozioziemski, A. G. MacPhee, A. Nikroo, H. F. Robey, J. D. Sater, and V. A. Smalyuk, "First measurements of fuel-ablator interface instability growth in inertial confinement fusion implosions on the National Ignition Facility," Phys. Rev. Lett **117**, 075002 (2016).
[18]J. Sanz, "Self-consistent analytical model of the Rayleigh-Taylor instability in inertial confinement fusion," Phys. Rev. Lett. **73**, 2700–2703 (1994).
[19]R. Betti, V. N. Goncharov, R. L. McCrory, P. Sorotokin, and C. P. Verdon, "Self-consistent stability analysis of ablation fronts in inertial confinement fusion," Phys. Plasmas **3**, 2122 (1996).
[20]R. Betti, V. N. Goncharov, R. L. McCrory, and C. P. Verdon, "Growth rates of the ablative Rayleigh–Taylor instability in inertial confinement fusion," Phys. Plasmas **5**, 1446 (1998).
[21]H. Takabe, K. Mima, L. Montierth, and R. Morse, "Self-consistent growth rate of the Rayleigh–Taylor instability in an ablatively accelerating plasma," Phys. Fluids **28**, 3676–3682 (1985).
[22]J. D. Kilkenny, S. G. Glendinning, S. W. Haan, B. A. Hammel, J. D. Lindl, D. Munro, B. A. Remington, S. V. Weber, J. P. Knauer, and C. P. Verdon, "A review of the ablative stabilization of the Rayleigh–Taylor instability in regimes relevant to inertial confinement fusion," Phys. Plasmas **1**, 1379–1389 (1994).
[23]V. Lobatchev and R. Betti, "Ablative stabilization of the deceleration phase Rayleigh-Taylor instability," Phys. Rev. Lett. **85**, 4522–4525 (2000).
[24]B. Srinivasan and X.-Z. Tang, "Mitigating hydrodynamic mix at the gas-ice interface with a combination of magnetic, ablative, and viscous stabilization," Europhys. Lett. **107**, 65001 (2014).
[25]S. W. Haan, "Onset of nonlinear saturation for Rayleigh-Taylor growth in the presence of a full spectrum of modes," Phys. Rev. A **39**, 5812–5825 (1989).

[26]S. W. Haan, "Weakly nonlinear hydrodynamic instabilities in inertial fusion," Phys. Fluids B **3**, 2349–2355 (1991).
[27]D. Layzer, "On the instability of superposed fluids in a gravitational field," Astrophys. J. **122**, 1 (1955).
[28]V. N. Goncharov, "Analytical model of nonlinear, single-mode, classical Rayleigh-Taylor instability at arbitrary Atwood numbers," Phys. Rev. Lett. **88**, 134502 (2002).
[29]J. Sanz, J. Ramírez, R. Ramis, R. Betti, and R. P. J. Town, "Nonlinear theory of the ablative Rayleigh-Taylor instability," Phys. Rev. Lett. **89**, 195002 (2002).
[30]J. Sanz, R. Betti, R. Ramis, and J. Ramírez, "Nonlinear theory of the ablative Rayleigh–Taylor instability," Plasma Phys. Controlled Fusion **46**, B367–B380 (2004).
[31]R. Betti and J. Sanz, "Bubble acceleration in the ablative Rayleigh-Taylor instability," Phys. Rev. Lett. **97**, 205002 (2006).
[32]R. Yan, R. Betti, J. Sanz, H. Aluie, B. Liu, and A. Frank, "Three-dimensional single-mode nonlinear ablative Rayleigh-Taylor instability," Phys. Plasmas **23**, 022701 (2016).
[33]S. X. Hu, V. A. Smalyuk, V. N. Goncharov, S. Skupsky, T. C. Sangster, D. D. Meyerhofer, and D. Shvarts, "Validation of thermal-transport modeling with direct-drive, planar-foil acceleration experiments on omega," Phys. Rev. Lett. **101**, 055002 (2008).
[34]L. Spitzer and R. Härm, "Transport phenomena in a completely ionized gas," Phys. Rev. **89**, 977–981 (1953).
[35]A. R. Bell, R. G. Evans, and D. J. Nicholas, "Elecron energy transport in steep temperature gradients in laser-produced plasmas," Phys. Rev. Lett. **46**, 243–246 (1981).
[36]M. Holec, J. Nikl, and S. Weber, "Nonlocal transport hydrodynamic model for laser heated plasmas," Phys. Plasmas **25**, 032704 (2018).
[37]W. A. Farmer, O. S. Jones, M. A. Barrios, D. J. Strozzi, J. M. Koning, G. D. Kerbel, D. E. Hinkel, J. D. Moody, L. J. Suter, D. A. Liedahl, N. Lemos, D. C. Eder, R. L. Kauffman, O. L. Landen, A. S. Moore, and M. B. Schneider, "Heat transport modeling of the dot spectroscopy platform on NIF," Plasma Phys. Controlled Fusion **60**, 044009 (2018).
[38]R. J. Henchen, M. Sherlock, W. Rozmus, J. Katz, D. Cao, J. P. Palastro, and D. H. Froula, "Observation of nonlocal heat flux using Thomson scattering," Phys. Rev. Lett. **121**, 125001 (2018).
[39]K. Shigemori, H. Azechi, M. Nakai, M. Honda, K. Meguro, N. Miyanaga, H. Takabe, and K. Mima, "Measurements of Rayleigh-Taylor growth rate of planar targets irradiated directly by partially coherent light," Phys. Rev. Lett. **78**, 250–253 (1997).
[40]H. Azechi, M. Nakai, K. Shigemori, N. Miyanaga, H. Shiraga, H. Nishimura, M. Honda, R. Ishizaki, J. G. Wouchuk, H. Takabe *et al.*, "Direct-drive hydrodynamic instability experiments on the GEKKO XII laser," Phys. Plasmas **4**, 4079–4089 (1997).
[41]S. G. Glendinning, S. N. Dixit, B. A. Hammel, D. H. Kalantar, M. H. Key, J. D. Kilkenny, J. P. Knauer, D. M. Pennington, B. A. Remington, R. J. Wallace, and S. V. Weber, "Measurement of a dispersion curve for linear-regime Rayleigh-Taylor growth rates in laser-driven planar targets," Phys. Rev. Lett. **78**, 3318–3321 (1997).
[42]T. Sakaiya, H. Azechi, M. Matsuoka, N. Izumi, M. Nakai, K. Shigemori, H. Shiraga, A. Sunahara, H. Takabe, and T. Yamanaka, "Ablative Rayleigh-Taylor instability at short wavelengths observed with moiré interferometry," Phys. Rev. Lett. **88**, 145003 (2002).
[43]V. A. Smalyuk, S. X. Hu, V. N. Goncharov, D. D. Meyerhofer, T. C. Sangster, D. Shvarts, C. Stoeckl, B. Yaakobi, J. A. Frenje, and R. D. Petrasso, "Rayleigh-Taylor growth stabilization in direct-drive plastic targets at laser intensities of $\sim 1 \times 10^{15}$ W/cm^2," Phys. Rev. Lett. **101**, 025002 (2008).
[44]M. Honda, K. Mima, K. Shigemori, M. Nakai, H. Azechi, and A. Nishiguchi, "Effects of non-local electron thermal transport on ablative Rayleigh-Taylor instability," Fusion Eng. Des. **44**, 205–208 (1999).
[45]R. C. Malone, R. L. McCrory, and R. L. Morse, "Indications of strongly flux-limited electron thermal conduction in laser-target experiments," Phys. Rev. Lett. **34**, 721 (1975).
[46]G. P. Schurtz, P. D. Nicolaï, and M. Busquet, "A nonlocal electron conduction model for multidimensional radiation hydrodynamics codes," Phys. Plasmas **7**, 4238–4249 (2000).
[47]P. L. Bhatnagar, E. P. Gross, and M. Krook, "A model for collision processes in gases. I. Small amplitude processes in charged and neutral one-component systems," Phys. Rev. **94**, 511–525 (1954).
[48]A. Marocchino, M. Tzoufras, S. Atzeni, A. Schiavi, P. D. Nicolaï, J. Mallet, V. Tikhonchuk, and J.-L. Feugeas, "Comparison for non-local hydrodynamic thermal conduction models," Phys. Plasmas **20**, 022702 (2013).
[49]M. Sherlock, J. P. Brodrick, and C. P. Ridgers, "A comparison of non-local electron transport models for laser-plasmas relevant to inertial confinement fusion," Phys. Plasmas **24**, 082706 (2017).
[50]J. P. Brodrick, R. J. Kingham, M. M. Marinak, M. V. Patel, A. V. Chankin, J. T. Omotani, M. V. Umansky, D. Del Sorbo, B. Dudson, J. T. Parker *et al.*, "Testing nonlocal models of electron thermal conduction for magnetic and inertial confinement fusion applications," Phys. Plasmas **24**, 092309 (2017).
[51]D. Cao, G. Moses, and J. Delettrez, "Improved non-local electron thermal transport model for two-dimensional radiation hydrodynamics simulations," Phys. Plasmas **22**, 082308 (2015).
[52]H. Zhang, R. Betti, V. Gopalaswamy, R. Yan, and H. Aluie, "Nonlinear excitation of the ablative Rayleigh-Taylor instability for all wave numbers," Phys. Rev. E **97**, 011203(R) (2018).
[53]H. Zhang, R. Betti, R. Yan, D. Zhao, D. Shvarts, and H. Aluie, "Self-similar multimode bubble-front evolution of the ablative Rayleigh-Taylor instability in two and three dimensions," Phys. Rev. Lett. **121**, 185002 (2018).
[54]J. Xin, R. Yan, Z.-H. Wan, D.-J. Sun, J. Zheng, H. Zhang, H. Aluie, and R. Betti, "Two mode coupling of the ablative Rayleigh-Taylor instabilities," Phys. Plasmas **26**, 032703 (2019).
[55]B. Van Leer, "On the relation between the upwind-differencing schemes of Godunov, Engquist–Osher and Roe," SIAM J. Sci. Stat. Comput. **5**, 1–20 (1984).
[56]E. F. Toro, M. Spruce, and W. Speares, "Restoration of the contact surface in the HLL-Riemann solver," Shock Waves **4**, 25–34 (1994).
[57]J.-L. Feugeas, P. Nicolaï, X. Ribeyre, G. Schurtz, V. Tikhonchuk, and M. Grech, "Modeling of two-dimensional effects in hot spot relaxation in laser-produced plasmas," Phys. Plasmas **15**, 062701 (2008).
[58]K. Otani, K. Shigemori, T. Sakaiya, S. Fujioka, A. Sunahara, M. Nakai, H. Shiraga, H. Azechi, and K. Mima, "Reduction of the Rayleigh-Taylor instability growth with cocktail color irradiation," Phys. Plasmas **14**, 122702 (2007).
[59]M. J.-E. Manuel, C. K. Li, F. H. Séguin, J. Frenje, D. T. Casey, R. D. Petrasso, S. X. Hu, R. Betti, J. D. Hager, D. D. Meyerhofer, and V. A. Smalyuk, "First measurements of Rayleigh-Taylor-induced magnetic fields in laser-produced plasmas," Phys. Rev. Lett. **108**, 255006 (2012).
[60]B. Srinivasan, G. Dimonte, and X.-Z. Tang, "Magnetic field generation in Rayleigh-Taylor unstable inertial confinement fusion plasmas," Phys. Rev. Lett. **108**, 165002 (2012).
[61]G. Schurtz, S. Gary, S. Hulin, C. Chenais-Popovics, J. C. Gauthier, F. Thais, J. Breil, F. Durut, J. L. Feugeas, P. H. Maire, P. Nicolaï, O. Peyrusse, C. Reverdin, G. Soullié, V. Tikhonchuk, B. Villette, and C. Fourment, "Revisiting nonlocal electron-energy transport in inertial-fusion conditions," Phys. Rev. Lett. **98**, 095002 (2007).